Research Article

Journal of Environmental Nanotechnology

Synthesis, Characterization, Directional Crystal Growth Mechanism and Photocatalytic Activity of Three-Dimensional Hierarchical Fern-Like Nanostructures of $BaTiO_3$

M. P. Nithya, L. Gomathi Devi*

Department of Post-Graduate Studies in Chemistry, Central College City Campus, Bangalore, KA, India

Received: 10.07.2018 Accepted: 14.08.2018

*gomatidevi_naik@yahoo.co.in

ABSTRACT

$BaTiO_3$ with fern-like nano-structural morphology has been successfully synthesized via a simple sol-gel method followed by an ageing process and was characterized by X-ray powder diffraction (PXRD) and Raman spectroscopy. The composition and the morphology were confirmed by scanning electron microscopy (SEM) with Energy-dispersive X-ray spectroscopy and (high-resolution) transmission electron microscopy (TEM/HRTEM). The bonding linkage between Ba, Ti and O in the $BaTiO_3$ sample was obtained by FTIR study. The bandgap was calculated by using the Kubelka-Munk function based on UV-absorption spectroscopic studies. The binding state of the elements present in $BaTiO_3$ was obtained from XPS analysis. The details pertaining to the thermal decomposition process of the uncalcined barium titanyl oxalate to barium titanate was obtained from TGA analysis. The surface area was determined by BET adsorption-desorption isotherms. The plausible directional growth mechanism of different $BaTiO_3$ facets forming fern-like clusters is discussed in detail. The fern-like $BaTiO_3$ exhibited only~10% higher photocatalytic activity compared to the $BaTiO_3$ with coral-like morphology for the degradation of methyl orange (MO) dye under UV irradiation. The photocatalytic degradation was also explored by the addition of H_2O_2 as electron scavenger, KI as surface hydroxyl radical scavenger and TBA as bulk hydroxyl radical scavenger.

Keywords: Fern-like $BaTiO_3$**;** $BaTiO_3$; Three-dimensional Nanostructure; Photocatalytic activity dendritic growth mechanism.

1. INTRODUCTION

Fabrication of a variety of structures like nanoparticles, nanocubes, nanorods, nanowires, and nanotubes are distinguished by their three-dimensional structure and can be correlated to their reactivity in various reactions. The formation of nanostructures and their properties are dependent on various factors like the chemical composition, phase, size, shape and their assemblies (Jing *et al.* 2009). These materials are extensively used in memory, transducers, sensors and energy-harvesting devices. (Zhao *et al.* 2010). The majority of low-temperature synthesis routes produce spherical $BaTiO_3$ particles with a cubic crystal structure. Elongated and other shape-controlled $BaTiO_3$ particles were normally prepared by employing a template. Extensive interest is shown by the researchers in the fabrication methods of various nanostructures of $BaTiO_3$, especially by simple preparative techniques (Marjeta *et al.* 2013). Synthesis of nanostructured $BaTiO_3$ with different morphologies such as plant-like (Zhou *et al.* 2007), cocoon-like (Feng *et al.* 2007), bowl-like (Zhao *et al.* 2010), single-crystal and coral-like $BaTiO_3$ (Edrissi *et al.* 2010) prepared by a hydrothermal technique by varying the precursors is reported in the literature (Zhao *et al.* 2010). Flower-like $BaTiO_3/Fe_3O_4$ hierarchically structured composite particles composed of nano-scale structures on microscale materials were synthesized by a simple solvothermal approach (Baoxiang *et al.* 2013). Synthesis of needle-like $BaTiO_3$ particles was obtained from the thermal decomposition of citrate precursor under temperature-controlled reaction conditions (Luis *et al.* 2003). The star-like, single-crystalline $BaTiO_3$ particles were grown from the alkaline aqueous solutions of sodium titanate and the aerogel TiO_2 (Marjeta *et al.* 2013). Sphere-like and confetti-like particles of $BaTiO_3$ were prepared under ultrasonic irradiation conditions (Feng *et al.* 2010). $BaTiO_3$ prepared from sol-gel method generally shows morphologies such as nanofibers (Junhan *et al.* 2007), colloidal sphere arrays (Zhibin *et al.* 2000), monoliths (Marjeta *et al.* 2013), nanorods (Zhang *et al.* 2008) and thin films (Adikary *et al.* 2003). There are no reports in the literature that shows the dendritic growth of $BaTiO_3$ nanostructures from a simple sol-gel method. These materials are extensively used in memory, transducers, sensors and energy-harvesting devices (Edrissi *et al.* 2010). The large-scale periodical forest of ferns with 3D architecture makes the material a

potential candidate for applications in ultra-sensitive gas sensing and exciton based photonic devices (Baoxiang *et al.* 2013). The dendritic nanostructures with hyper branching have drawn the attention of our research group, and an attempt is made in understanding the facts related to fractal growth and their potential applications as a photocatalyst. Hierarchically self-assembled fractal patterns of $BaTiO_3$ has shown that the distinct size, shape, and chemical functionality of such structures make them promising candidates for the design and fabrication of new functional nanomaterials (Minhua *et al.* 2005). However, these studies mainly deal with the structural characterization of $BaTiO_3$ and no information is provided regarding the mechanism involved in the anisotropic crystal growth. In addition, the dendritic growth patterns have been produced using facile techniques such as electrodeposition and the hydrothermal process. In this study, we report the synthesis of novel three dimensional (3D) $BaTiO_3$ nanoparticles with fern-like structure with exquisite fractal features via a simple sol-gel method.

2. EXPERIMENTAL SECTION

2.1 Materials

Titanium (IV) chloride ($TiCl_4 \geq 99.9\%$) is obtained from Merck Chemicals Limited, and Barium Chloride and Oxalic acid dehydrate is obtained from British Drug Houses (India) Pvt Limited, and Methyl Orange (MO) is from SDFCL fine-chem limited. Double distilled water was used throughout the experiments.

2.2 Catalyst Preparation

The adopted preparation technique is very much similar to the method reported in the previous studies except for ageing the precipitate for preferential crystal growth of $BaTiO_3$ in definite directions (Devi *et al.* 2018). $BaTiO_3$ was prepared by sol-gel method by using diluted $TiCl_4$ and $BaCl_2$. The concentrated $TiCl_4$ solution is diluted, and its titanium content is determined to an aliquot solution containing 6.5 g of titanium, a solution containing 32 g of $BaCl_2$. $2H_2O$ dissolved in 320 ml of water is added. The above mixture was added dropwise to a hot (80˚C) well-stirred solution of oxalic acid (37 g of dehydrating salt dissolved in 320 ml of water). A crystalline precipitate of barium titanyl oxalate is obtained, and it is allowed to age for 40 days to obtain dendritic fern-like $BaTiO_3$. This precipitate was washed several times to remove all the chloride ions and was further air-dried. The obtained barium titanyl oxalate was calcined at 700˚C for 4 hrs to obtain $BaTiO_3$.

2.3 Instruments used for the Characterisation of the Catalyst

The powder X-ray diffraction (PXRD) patterns were obtained using the Panalytical X'pert Pro MPD diffractometer, which was operated at 30 gkV and 20 mA using Cu K α with a nickel filter. The scan rate was varied from 2˚ to 0.5˚/ min to get X-ray diffraction line broadening. The Fourier transform infrared (FTIR) spectra were obtained using Thermo Avtar 370 spectrometer with KBr as the standard. The Diffuse Reflectance Spectra (DRS) of the photocatalyst was obtained using Schimadzu-UV 3101 PC UV-VIS-NIR UV-Visible spectrophotometer with $BaSO_4$ as the reference standard. The absorbance data were transformed into reflectance values, and Kubelka–Munk method is used for the bandgap measurement. The surface morphology was analysed by scanning electron microscopic (SEM) and EDX analysis using ULTRA 55 microscope operating at 25 kV on the specimen upon which a thin layer of platinum had been evaporated. An electron microprobe is used in the EDX mode. Transmission electron microscopy (TEM) studies were performed in a Titan G2 60 300 TEM operated at 200 kV, equipped with an EDS detector. The TEM samples were dispersed in ethanol and then collected in a carbon grid. The Raman spectra were recorded on a WITEC model CRC200, using a 5.5 mW laser with a wavelength of 514.5 nm.

The specific surface area of the powders was measured by dynamic Brunnere Emmette Teller (BET) method in which N_2 gas was adsorbed at 77 K using Digisorb 2006 surface area, pore volume analyser Nova Quanta Chrome Corporation instrument multipoint BET adsorption system. The X-ray photoelectron spectroscopy (XPS) measurements were carried out using AXIS ULTRA from AXIS 165, integrated with Kratos patented Magnetic immersion lens, charge neutralization system and spherical mirror analyser. The spherical mirror analyser provides real-time chemical state and elemental imaging using the full range of pass energies and multi-point analysis from either real-time or scanned images without the need for a sample translation. All binding energies were calibrated to the C 1s peak at 284.8 eV of the surface adventitious carbon. The residual concentration of the MO during the degradation reaction process was measured by using T80 UV/VIS UV-spectrometer, PG Instruments Ltd, in the region of maximum absorption (200–800 nm). TG and DTA analysis were performed in order to record the thermal changes of the sample TGA instruments were performed in Metlar TA 4000 instrument operated under nitrogen flow in the temperature range of RT-800 °C with a heating rate of 20 °C/min.

3. RESULTS & DISCUSSION

3.1.PXRD Studies

The PXRD patterns of $BaTiO_3$ are shown in Fig. 1. The pattern shows peaks at 2θ values of 22.17º (001), 31.59º (101), 39.07º (111), 45.30º (200), 50.92º (210), 56.32º (211), 65.86º (220), 70.52º (212), 75.06º (310),

79.22º (311), (the number in the parenthesis indicates the *hkl* values). All the observed peaks can be indexed to a pure tetragonal phase of $BaTiO_3$ which were consistent with the standard data (JCPDS File no. 75-2120) (Devi *et al.* 2018). The average crystallite size was estimated for $BaTiO_3$ based on the broadening of (101) peak at 2θ=31.61º using the Scherrer's equation:

$$D = \frac{k\lambda}{\beta cos\theta} \quad (1)$$

Where λ is the wavelength of the graphite-filtered Cu Kα source used (λ=1.541 Å), β is the full width at half maximum (FWHM) of (101) and (110) diffraction angles, k is a shape factor (0.94), and θ is the angle of diffraction. The average crystallite size was estimated to be 42.8 nm. The lattice strain was calculated from the following equation:

$$\varepsilon = \frac{\beta}{4\tan\theta} \quad (2)$$

Where ε is the lattice strain, β is the full width at half maximum (FWHM) of the (101) diffraction plane, and θ is the angle of diffraction. The lattice strain was found to be 0.00862 for $BaTiO_3$. The cell parameters were calculated by using the X-ray diffraction peaks of the crystal planes by using the following equations:

$$d_{hkl} = \frac{\lambda}{2\sin\theta} \quad (3)$$

$$\frac{1}{d_{hkl}^2} = \frac{h^2}{a^2} + \frac{k^2}{b^2} + \frac{l^2}{c^2} \quad (4)$$

d_{hkl} Is the distance between crystal planes of *(h k l)*, λ is X-ray wavelength, θ is diffraction angle of crystal plane *(h k l)*, and a, b, c are the lattice parameters. The calculated cell parameters and the cell volume is represented in Table 1.

Table 1. The Phase Composition, the Crystallite Size (D), Lattice Parameters (A), Cell Volume (V) and Lattice Strain (ε) of $BaTiO_3$

Sample	$BaTiO_3$
Phase composition	Tetragonal
D (nm)	42.8
A in Å	a=b=3.954, c=4.006
V (Å)³	62.6
ε	0.00862

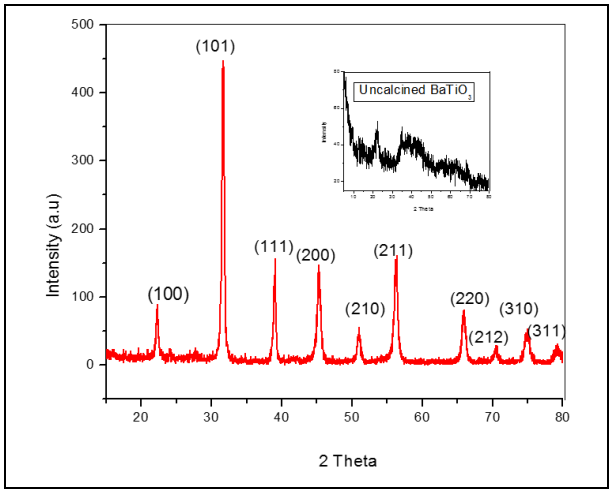

Fig. 1: PXRD Pattern of $BaTiO_3$

3.2 UV-Visible Absorbance Spectral Studies

The optical absorption properties of $BaTiO_3$ was investigated by the DRS studies. The results obtained by DRS studies are used to investigate the electronic band structure of $BaTiO_3$.The bandgap energy (E_g) of each catalyst was determined by using Kubelka–Munk function. The intercepts of the tangents to the plots of (F (R_∞). E^2) versus photon energy (E) are shown in Fig. 2. The Kubelka–Munk function F (R_∞) and photon energy (E) can be calculated by following (Kavitha *et al.* 2014):

$$F(R_\infty) = \frac{(1-R_\infty)^2}{2R_\infty} \quad (5)$$

$$R_\infty = 10^{-A} \quad (6)$$

$$E = \frac{1240}{\lambda} \quad (7)$$

where R_∞ is the reflection coefficient of the sample, A is absorbance intensity of $BaTiO_3$ and λ is absorption wavelength. The optical absorption threshold of the sample was approximately 394.9nm, corresponding to the bandgap of 3.14 eV, and no absorption was observed in the visible region.

3.3 FTIR Analysis

The FTIR spectra of $BaTiO_3$ in the range of 500 - 4000 cm^{-1} is shown in Fig. 3. The O-H stretching vibrations of the interlayer water molecules are observed as a broad and strong band centred at 3435 cm^{-1}. The peak observed at 1634 cm^{-1} can be assigned to the bending vibration of water molecules. These peaks are invariantly present on the surface of transition metal oxides (Fig. 4) and conventionally considered as an important factor in affecting the surface properties of the metal oxide(Lei *et al.* 2013). The band at 570 cm^{-1} can correspond to the Ti-O stretching vibration (Jenq-dar *et al.*1999). The peak

observed at 1444 cm^{-1} is a characteristic band of the crystalline barium titanate (Ba-Ti-O) (Yury *et al.* 2007).

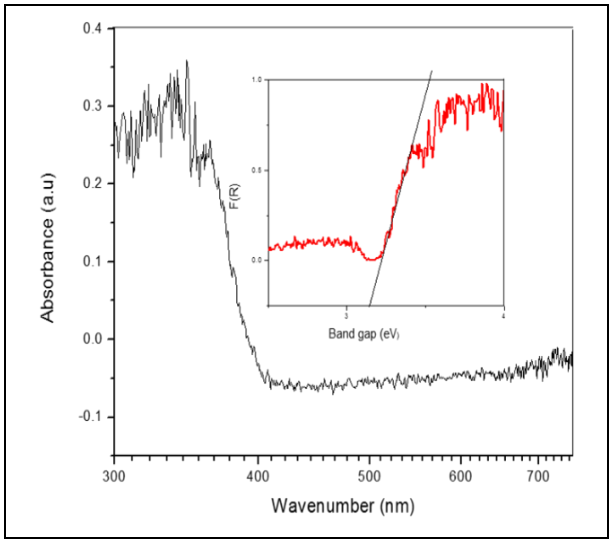

Fig. 2: UV-Vis Absorbance Spectra of $BaTiO_3$

3.4 Thermogravimetry (TG) and Differential Thermal Analysis (DTA)

The thermograms obtained from TGA and DTA analysis under nitrogen atmosphere are shown in Fig. 4. The thermal decomposition step may be described by three distinct weight loss process. The first weight loss occurs around 200 ±℃, which corresponds to the vaporization of water molecules that are trapped in the gel and corresponds to the endothermic peak in the DTA curve at that temperature. The second weight loss process occurs between 250 to 400 ±℃, which is attributed to the pyrolysis of oxalate residues and is indicated by a prominent exothermic peak in the DTA curve (Michael *et al.* 2000). The third and final weight loss occurs between 600 to 800±℃, which requires a higher temperature that corresponds to the complete combustion of barium titanyl oxalate and also the release of CO_2. The DTA exothermic shoulder peak at approximately at 680℃ is believed to be due to phase transition from amorphous gel to polycrystalline tetragonal $BaTiO_3$.The de-composition process in the nitrogen atmosphere can be summarized as follows (Jianfei *et al.*1999):

$$BaTiO(C_2O_4)_2.4H_2O \xrightarrow{40\text{-}250^oC} BaTiO(C_2O_4)_2 + 4H_2O \quad (8)$$

$$2BaTiO(C_2O_4)_2 \xrightarrow{180\text{-}250^oC} Ba_2Ti_2O_2(C_2O_4)_3CO_3 + CO \quad (9)$$

$$Ba_2Ti_2O_2(C_2O_4)_3CO_3 \xrightarrow{250\text{-}460^oC} Ba_2Ti_2O_5CO_3(CO_2) + 3CO + 2CO_2 \quad (10)$$

$$Ba_2Ti_2O_5CO_3(CO_2) \xrightarrow{450\text{-}600^oC} Ba_2Ti_2O_5CO_3 + CO_2 \quad (11)$$

$$Ba_2Ti_2O_5CO_3 \xrightarrow{600\text{-}750^oC} 2BaTiO_3 + CO_2 \quad (12)$$

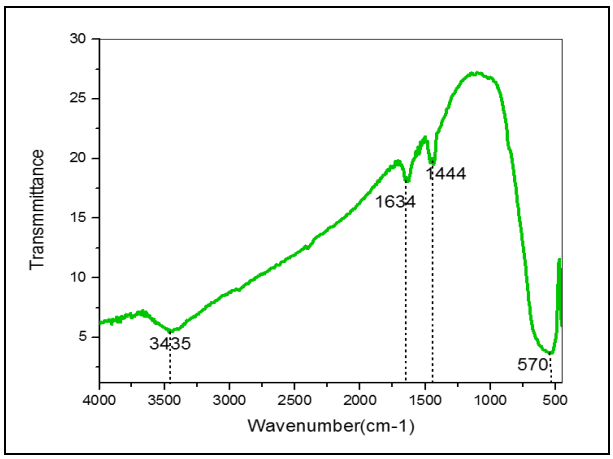

Fig. 3: FTIR Spectrum of $BaTiO_3$

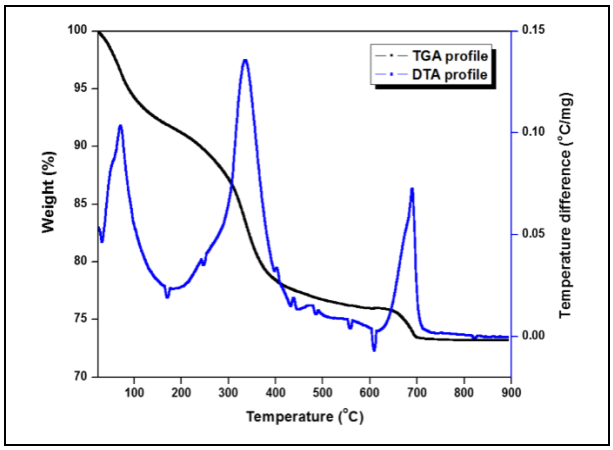

Fig. 4: TG and DTA Curves of $BaTiO_3$

3.5 SEM and EDX Analysis

SEM images of $BaTiO_3$ clusters with a dendritic growth are presented in Fig. 5. The structure consists of a 3D architecture of a fern. The length of an average stem is 19.24 µm and the leaflet is 6.093 µm. The width of an average leaflet was also calculated and was found to be 2.502 µm. The angle between the stem and the leaf is ~75 – 79°. The fixed angle between the leaflets and the stem indicates that the growth is diffusion-controlled and accomplished through oriented growth. This type of oriented growth occurs due to the dislocations that occur during the growth of the crystals (Samanta *et al.* 2011; Yu-Fong *et al.* 2012). The fern leaves emerge from the faces possessing high surface energy from the tetrahedron central core growing in the outward direction, and the growth occurs until the width of the leaves become smaller and reaches the tips where the surface energy is lowered. Thus, mass transport limited branching growth is promoted. The growth is such that the apexes of the crystal protrude into the region of higher concentration and the growth occurs up to the state of depletion of ions and molecules that feed the growth at the crystal/solution interface. Thus, the apexes can grow

faster than the rest of the facets to form branches (Samanta *et al.* 2011). Qualitative and quantitative determination of contents in the prepared sample was studied by EDX technique as shown in Fig. 4 (a) by using grid supported carbon film of 15–25 nm thickness which gives exceptionally low background. The weight % values for $BaTiO_3$ is represented in Table 2.

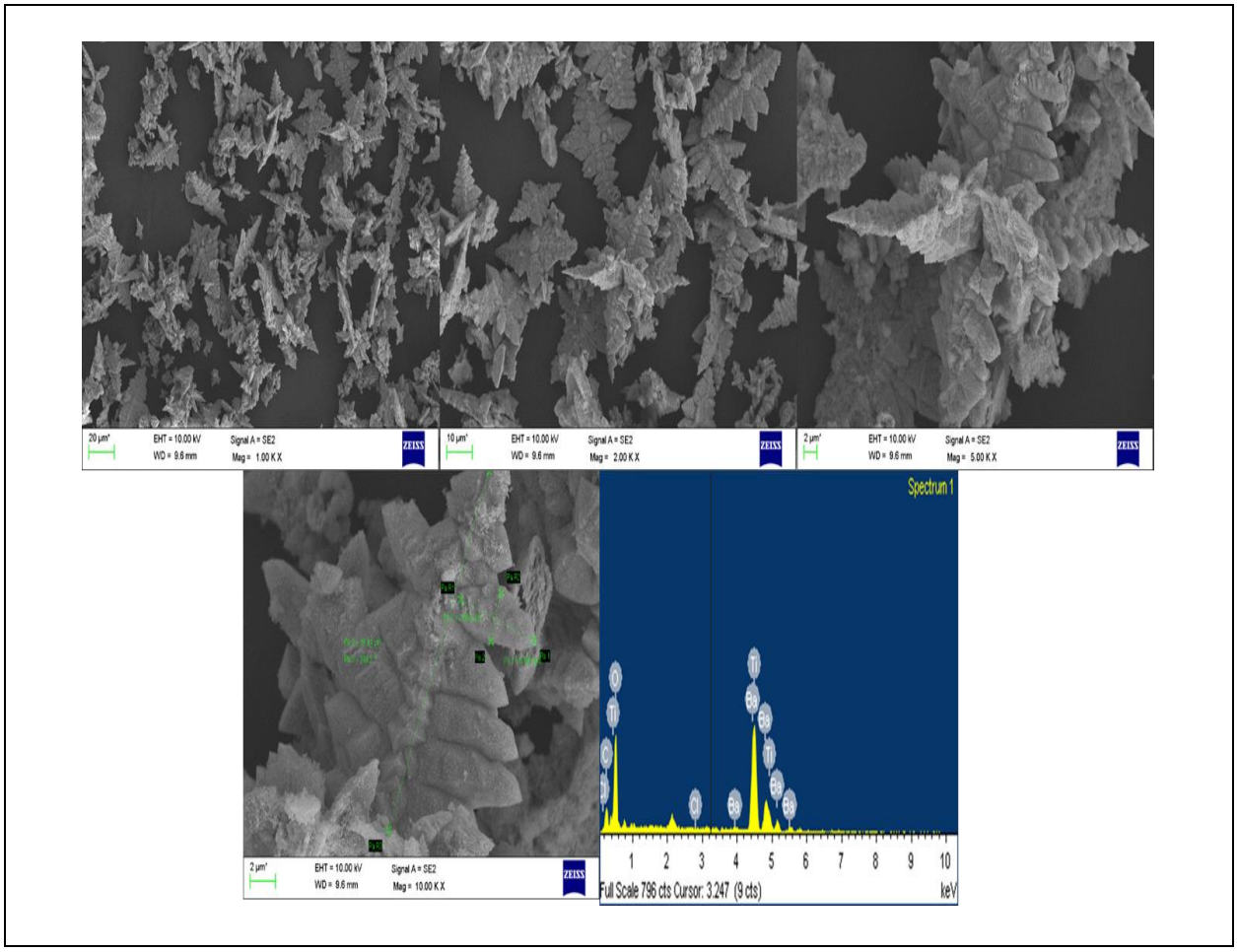

Fig. 5: SEM Images and EDX Spectra of $BaTiO_3$

Table 2. EDX Analysis of $BaTiO_3$

Element	$BaTiO_3$ Weight %
Barium titanate (Ba)	50.15
Titanium (Ti)	23.05
Oxygen (O)	26.80
Total	100.0

3.6 TEM Analysis

TEM observations revealed that the fern-like structures were characterized as being aggregates of nanoparticles, with the primary particle size being 58 nm. The particle size distribution was calculated by fitting the histograms with Gaussian functions Fig. 6 (b) (Barbosa *et al.* 2011). The aggregated clusters showed a single crystalline structure which was very well-identified by the selected area electron microscope (SAED) pattern. This means that each leaf of the fern was composed of oriented nanocrystals and the assembly of these nanocrystals occurs by attachment between specific crystal faces. Fig. 6(a) shows the TEM image of a single leaf of a fern. Fig. 6(b) shows the HRTEM image of one single particle with the distances of 4.03 and 3.99 A ° of lattice fringes which can be indexed to the (001) plane and (010) plane of tetragonal $BaTiO_3$, respectively. The SAED pattern, which can be indexed to tetragonal $BaTiO_3$ is shown in Fig. 6(c).

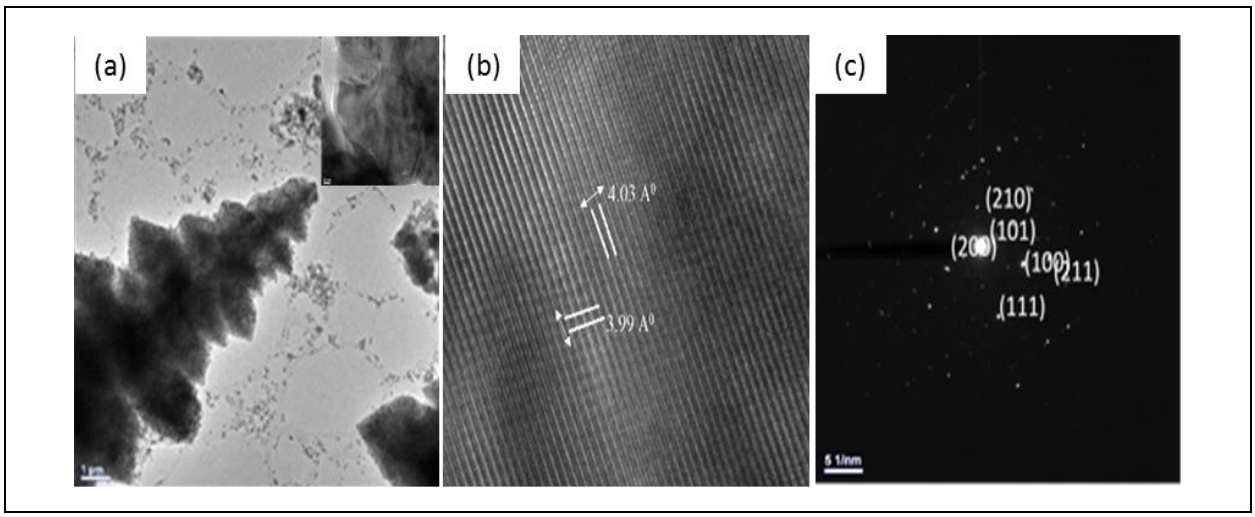

Fig. 6 (a, b, c): TEM and HRTEM Images of $BaTiO_3$

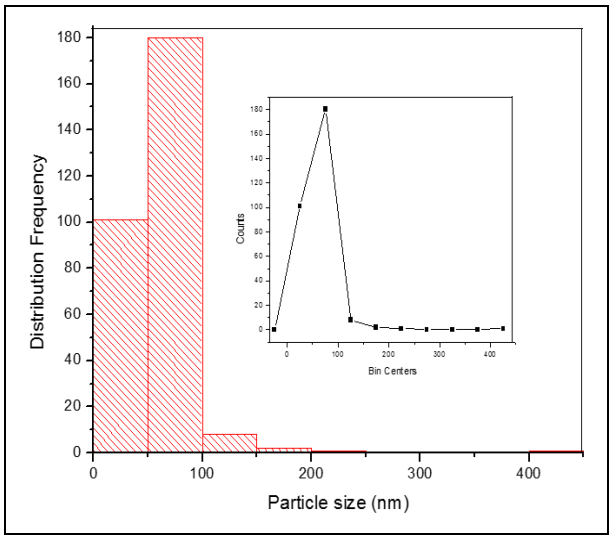

Fig. 6(d): Histograms of the Grain Sizes, Determined from the TEM Micrographs

3.7 Plausible Growth Mechanism

It is well known that the growth of a crystal depends on a number of parameters like type of solvent, type of precursor, nucleation sites, mechanical barriers and time. Factors such as surface chemistry, hydrophobicity and surface charge can also greatly influence the morphology of the metal particles. The growth mechanisms can be explained on the basis of mass transport and diffusion transport limited processes and reaction limited fractal aggregation reactions (Harale *et al.* 2013). The surface energy of different crystalline planes determines the habit formation route of a crystal. In cases where deposition of the growth species is limited through diffusion or growth potential, edges and corners protruding into higher concentration regions of the growth solution may experience faster growth than the natural habit planes (Barbosa *et al.* 2011). In the cases of dendritic nanostructures, the ensuing morphology is conciliation between the inherent crystal structure of the material and the kinetic factors employed during the synthetic route. In the present case, kinetic factors were not changed. Hence, the growth observed on certain planes becomes energetically favourable when the surface tensions of those planes are more and the total energy of the system becomes less (Vivek *et al.* 2009). The anisotropic growth occurs as a result of fine-tuning of the surface tensions of those planes as well as by the alterations that occur in the experimental conditions, such as substrate concentration, reaction temperature, and time. In the present case, surface tensions were invariably present within the system, which lead to the anisotropic growth and the reaction condition is such that the mixture was allowed to age for a long duration (Samanta *et al.* 2011). Mass-transport-limited growth is another source of anisometricdevelopment of nanoparticles. If interfacial processes are extremely fast during a crystal-growth process, the long-range transport of mass controls the rate of growth. Defined shapes, dendritic or branch formation are formed due to high supersaturation conditions, which disturb the equilibrium.

The fast interfacial process creates a depletion zone around a crystal at the crystal/solution interface due to the fast accommodation of the growth units (atoms, ions, molecules), and the supersaturation increases with distance into the parent phase. When a depletion zone is formed around a crystal with a polyhedron shape, the apexes of the crystal protrude into the region of higher concentration. Consequently, the rate of growth of any apex (protrusion) will be greater than the growth rate of the rest of the crystal facets, leading to the formation of branches. The diffusive nature of long-range transport processes gives rise to such morphological instabilities, leading to shapes like dendrites. At very high supersaturations, morphological instability can occur and dendritic, cellular, Hopper, etc., growth forms may appear (Tapan *et al.* 2010). Dendritic crystal growth patterns have remarkable connectivity between the

crystals, which are formed by the hierarchical self-assembly under the non-equilibrium conditions.

3.8 XPS Analysis

XPS measurements were carried out in order to investigate the chemical environment and binding state of the elements. Fig. 7 (a) represents the survey spectrum of $BaTiO_3$ sample showing Ba, Ti, O, and C peaks which is very much similar to the reported literature(Yong *et al.* 2006). The C element is ascribed to adventitious hydrocarbon in carbon tape from XPS instrument itself. The high-resolution XPS spectrum of barium (Fig. 7(b)) shows the doublet feature with binding energy (B E) peaks at approximately 795.7 eV and 780 eV, which could be ascribed to the splitting of the Ba $3d_{3/2}$ and Ba $3d_{5/2}$ spin states, respectively which is in good agreement with the reported data (Chia-Yu *et al.* 2011). Fig. 7(c) represents the high-resolution XPS spectrum of titanium with two peaks at approximately 458.35 eV, and 464.1 eV can be recognized and assigned to the distinct Ti $2p_{3/2}$ and Ti $2p_{1/2}$ signals for the chemical state of Ti in Ti^{4+} (Miot *et al.* 1997; Markus *et al.* 2004). In addition, an O1s peak at 532.5 eV is seen in Fig.7 (d) (Nayak *et al.* 2014).

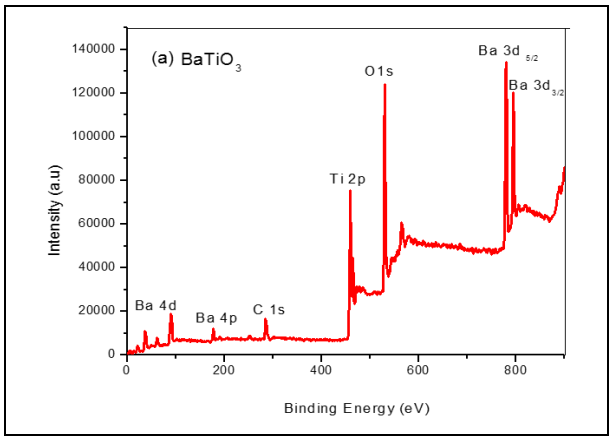

Fig. 7(a): The XPS Survey Spectra of $BaTiO_3$

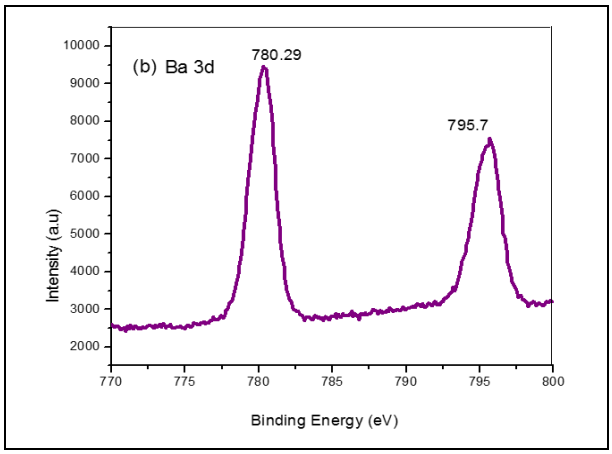

Fig. 7(b): Ba 3d XPS Spectra with 3d $_{3/2}$ & 3d $_{5/2}$ Spin States

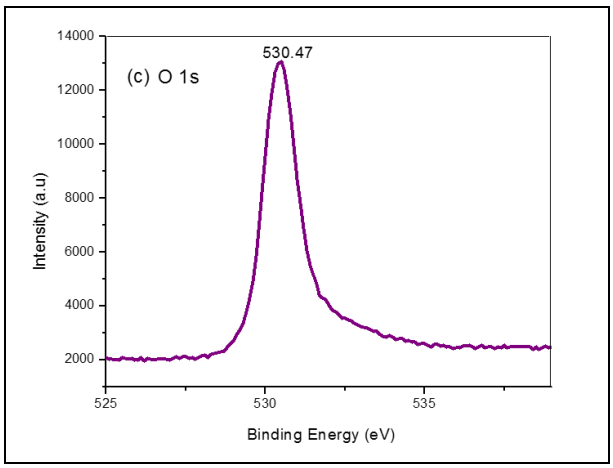

Fig. 7(c): Ti 2p XPS Spectra with $2p_{3/2}$ & $2p_{1/2}$

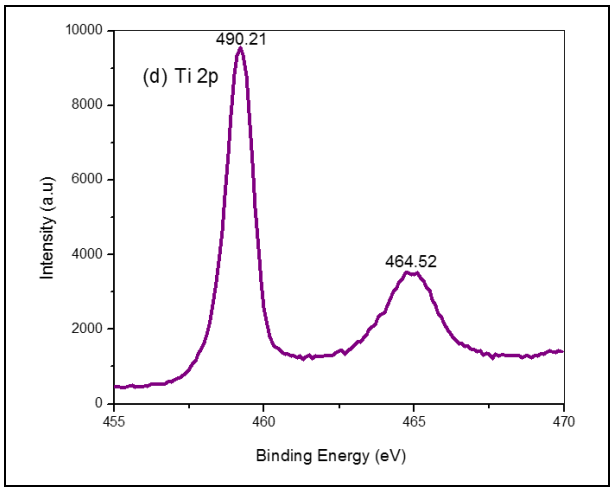

Fig. 7(d): O 1s XPS Spectra

3.9. BET Surface Analysis

Fig. 8 illustrates the N_2 adsorption-desorption isotherm of the prepared pure $BaTiO_3$ together with its corresponding pore size distribution profile. The pore size distribution was calculated from the desorption branch of a nitrogen isotherm by the BJH method (Devi *et al.* 2014). The mesoporous structure was confirmed by N_2 gas sorption, which shows type-IV adsorption isotherm with an elongated hysteresis. The occurrence of the hysteresis loop in the p/p_0 range starting from 0.533 - 0.928 exhibiting typical characteristic mesoporous structure. The prepared $BaTiO_3$ has a specific surface area of 24.45 m^2 g^{-1}. The pore size distribution measurement indicates that $BaTiO_3$ has a pronounced mesoporosity with a smaller particle size and larger specific surface area. The pore size distribution curve (shown in Fig. 4 inset) was obtained from the desorption branch of the isotherm by BJH method, for which the prepared sample displayed an average pore diameter of 183.632 Å and the average pore volume of 0.02690 cc/g. The average particle size, D_{BET} was estimated with the help of the equation (Vijatoic *et al.* 2008):

$$D_{BET} = \frac{6000}{\rho . S_{BET}} \quad (13)$$

Where ρ is the density (g/cm^3) of $BaTiO_3$ and S_{BET} is the surface area (m^2/g). The average particle size was found to be 40.7nm. The values of crystallite size calculated from the PXRD technique and the average particle size calculated from BET can be related in the following way (Mandal *et al.* 2007):

$$DA = \frac{D_{BET}}{D_{XRD}} \quad (14)$$

Where DA is the degree of agglomeration, and it was found to be approximately 0.95˚ (Kavitha *et al.* 2014).

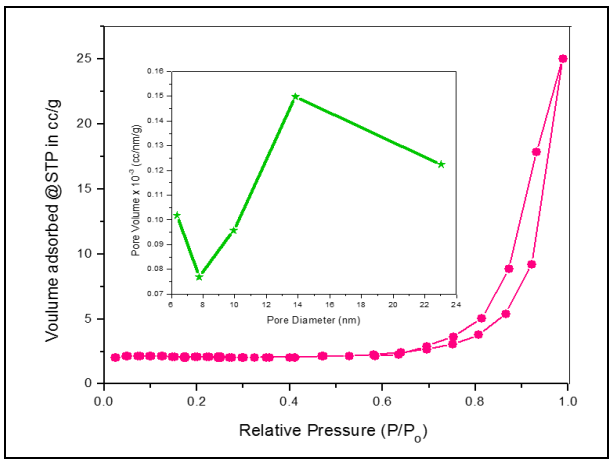

Fig. 8: The N_2 Adsorption-desorption Isotherms of $BaTiO_3$. The Figure in the Inset Shows BJH Pore Size Distribution Curve of $BaTiO_3$

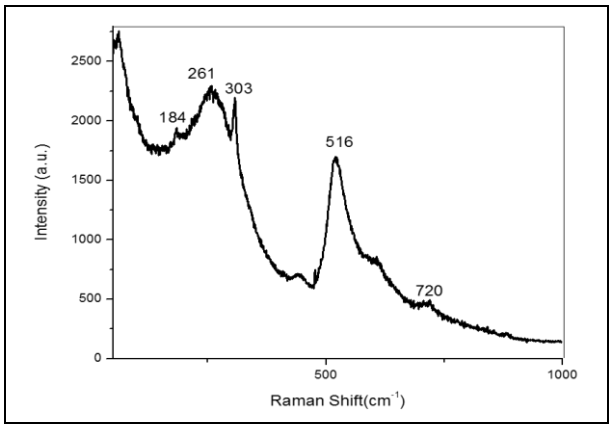

Fig. 9: Raman Spectra of $BaTiO_3$

3.10 Raman

The variation of crystal structure and the changes in the phase could be studied by Raman spectroscopy which is a sensitive technique. The Raman spectra were recorded in the wavelength range 100-800 cm^{-1}. It is well known that the cubic phase of $BaTiO_3$ is Raman inactive, and the tetragonal phase is found to be Raman active. The obtained spectra (Fig. 9) is characterized by five bands situated at 184, 261, 303, 516, and 720 cm^{-1}. Bands at 303 and 720 cm^{-1}can are used as the indication of the polarized tetragonal phase of $BaTiO_3$ (Margarita *et al.* 2009). It is accepted by many researchers that the Raman peak around 260 cm^{-1} is a characteristic peak of tetragonal $BaTiO_3$, which can vary with particle size, shape, and aggregation (Yang *et al.* 2011). The presence of the above-described bands confirm the tetragonal phase of $BaTiO_3$, and these results are further substantiated by the SAED pattern and PXRD results.

3.11 Photocatalytic Activity

The photocatalytic activity of fern-like $BaTiO_3$ was tested for the degradation of MO under the illumination of UV and solar light (Fig. 10 & Table 3). The degradation of MO under solar light is almost negligible since $BaTiO_3$ cannot be activated under solar light due to its wide bandgap. The plot of C/C_0 vs time for the degradation of MO with $BaTiO_3$ photocatalyst is shown in Fig. 10(a). The degradation of MO is found to be 74 % with a rate constant of 1.00 x10^{-2} min^{-1} in a time period of 150 min with fern-like $BaTiO_3$. For comparison, non-fern like $BaTiO_3$ was taken to study the photocatalytic activity. The % degradation and the rate constant for non-fern like $BaTiO_3$ was found to be 65 % and 0.74 x10^{-2} min^{-1} in a time period of 150 min (Devi *et al.* 2018). There is a remarkable enhancement in the rate of photocatalytic degradation by the addition of H_2O_2 as an oxidizing agent for the above reaction. Direct photolysis of H_2O_2 under UV light leads to the formation of reactive hydroxyl free radicals, a dominant species for enhancing the rate of the degradation reaction (Zhao *et al.* 2012). Further, H_2O_2 can also act as a better electron acceptor in addition to oxygen, thereby reduces the rate of electron-hole recombination. The enhancement of the degradation rate is almost eight times, and 98 % of degradation takes place in a time period of 60 min for the reaction with a time period of 60 min for the reaction with $BaTiO_3$ in the presence of H_2O_2.

3.12 Effect of Addition of Surface (KI) and Bulk (TBA) Hydroxyl Radical Scavengers on the Photocatalytic Activity

The rate of photocatalytic degradation is affected by the change in the concentration of both surface and bulk hydroxyl radicals. The degradation reaction was carried out in the presence of KI (surface hydroxyl radical scavenger) and TBA (bulk hydroxyl radical scavenger) (Fig. 10) (Morsi *et al.* 2000, Zhiqiao *et al.* 2008). KI and TBA are scavengers of VB hole and thereby hinders the process of formation of hydroxyl free radicals. It was observed that the extent of degradation decreased by the addition of KI by 10 % and TBA by 20

%, implying the major role of bulk hydroxyl radicals rather than surface hydroxyl radicals in the degradation reaction process.

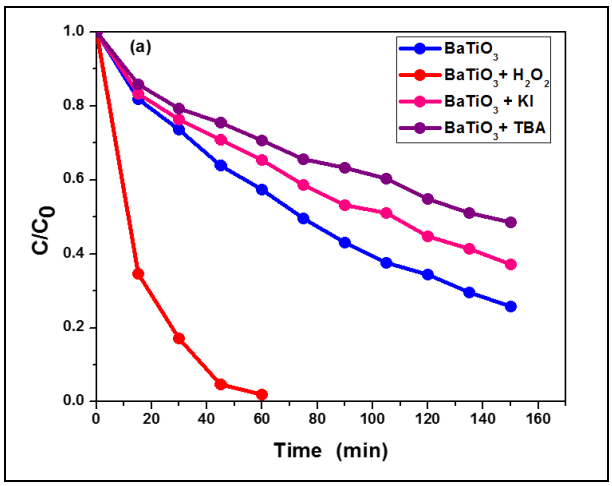

Fig. 10(a): The Plot of C/C_0 vs Time for the Photocatalytic Degradation of MO in the Presence of $BaTiO_3$, $BaTiO_3/H2O_2$, $BaTiO_3$/KI and $BaTiO_3$/TBA

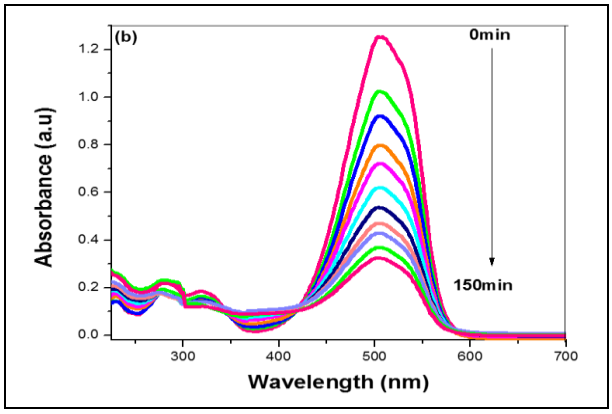

Fig. 10(b): UV-visible Absorbance Spectrum of MO Recorded at Different Time Intervals During the Process of Degradation for the Reaction with $BaTiO_3$

Table 2. Rate Constant Values and % Degradation of MO under UV Light Illumination

Photocatalyst	Rate constant (min^{-1}) x 10^{-2}	Time (min)	% Degradation
$BaTiO_3$	1.00	150	74
$BaTiO_3$ + TBA	0.44	150	51
$BaTiO_3$ + H_2O_2	6.56	60	98
$BaTiO_3$ + KI	0.62	150	63
$BaTiO_3$*	0.74	150	65

$BaTiO_3$*- non-fern like BTO

4. CONCLUSION

In summary, Fern-like $BaTiO_3$ nanostructures have been synthesized through a simple sol-gel method followed by continuous ageing of the reaction mixture for the dendritic growth. The tetragonal phase of the sample was confirmed by PXRD, Raman and SAED pattern from TEM analysis. The average particle size was found to be~ 58 nm. Photocatalytic studies revealed that the increase in photocatalytic activity of Fern-like $BaTiO_3$ was only marginal over that of non-fern like $BaTiO_3$ for the degradation of methyl orange under UV irradiation. 74% of MO was degraded within 150 min with a degradation rate of 1.00 x 10^{-2} min^{-1} for fern-like $BaTiO_3$. The % degradation and the rate constant for non-fern like $BaTiO_3$ was found to be 65 % and 0.74 x10^{-2} min^{-1} in a time period of 150 min. The presence of an electron acceptor like H_2O_2 can accelerate the electron transfer and inhibit the fast electron/hole recombination. The experiments with KI and TBA as surface and bulk hydroxyl radical scavengers show that the catalytic activity decreased by 20 % for TBA and by 10 % for KI. This implies the major contribution of bulk hydroxyl radicals compared to the surface hydroxyl radicals. The fern-like $BaTiO_3$ crystal morphology did not show major changes in the photocatalytic activity compared to non-fern like $BaTiO_3$.

ACKNOWLEDGEMENTS

The authors acknowledge UGC, DSA, SAP, the government of India for the funding.

REFERENCES

Adikary, S. U. and Chan, H. L.W., Ferroelectric and dielectric properties of sol-gel derived BaxSr1−xTiO3 thin films, Thin Solid Films, 424, 70-74, (2003). https://doi.org/S0040-6090(02)00918.5

Baoxiang, W., Yichao, Y., Chenjie, L., Shoushan, Y. and Kezheng, C., Synthesis of flower-like BaTiO3/Fe3O4 hierarchically structured particles and their electrorheological and magnetic properties. Dalton Trans., 42, 10042-10055, (2013). https://doi.org/10.1039/C3DT50504A

Barbosa, J.G., Pereira, M. R., Moura, C., Mendes, J. A. and Almeida, B. G., Barium titanate thin films deposited by electrophoresis on p-Doped Si (001) Substrates, J. Nanosci. Nanotechnol., 11, 8700-8704, (2011). https://doi.org/10.1166/jnn.2011.3494

Chia-Yu, W., Shu-Hao, K., Yu-Ming, H., Wen-Chieh, H., Feri, A. and Yeong-Her, W., High-mobility pentacene-based thin-film transistors with a solution-processed barium titanate insulator, IEEE Electron Device Lett., 32, 90-92 (2011). https://doi.org/10.1109/LED.2010.2084559

Devi, L. G. and Kavitha R., Enhanced photocatalytic activity of sulfur-doped TiO2 for the decomposition of phenol: A new insight into the bulk and surface modification. Mater. Chem. Phys., 143, 1300-1308, (2014). https://doi.org/10.1016/j.matchemphys.2013.11.038

Devi, L. G. and Nithya, P. M., Photocatalytic activity of Hemin (Fe (III) porphyrin) anchored BaTiO3 under the illumination of visible light: synergetic effects of photosensitization, photo-Fenton & photocatalysis processes, Inorg. Chem. Front., 1, 127-138, (2018). https://doi.org/10.1039/C7Q100590C

Devi, L. G. and Nithya, P. M., Preparation, characterization and photocatalytic activity of BaTiF6 and BaTiO3: A comparative study, J. Environ. Chem. Eng., 3, 3565-3573, (2018). https://doi.org/10.106/j.jece.2017.04.038

Edrissi, M. and Hosseinabadi, H. A., Sythesis of coral-like and spherical nanoparticles of barium titanate using factorial and Taguchi experimental design, Mat. Wiss. u. Werkstofftech., 41, 154-160, (2010). https://doi.org/10.1002/mawe.201000569

Feng, D., Kazumi, K., Hiroaki, I., Satoshi, W., Hajime, H., Makoto and Kuwabarae, Oriented aggregation of BaTiO3 nanocrystals and large particles in the ultrasonic-assistant synthesis, Cryst. Eng. Comm., 12, 3441-3444, (2010). https://doi.org/10.1039/C003587D

Feng. Q., Hirasawa, M., Kajiyoshi, K. and Yanagisawa, K., Hydrothermal soft chemical synthesis of BaTiO3 and titanium oxide with cocoon-like particle morphology, J. Mater. Sci., 42, 640-645, (2007). https://doi.org/10.1007/s10853-006-1142-0

Harale, N, S., Kamble, D. L., Gang, M. G., Rao, V. K., Kim, J. H. and Patil, P. S., Exotic fern-like morphologies, Mater. Today, 16, 452-453, (2013). https://doi.org/10.1016/j.mattod.2013.10.002

Jenq-dar, T. and Fang, T., Effects of molar ratio of citric acid to cations and of pH value on the formation and thermal-decomposition behavior of barium titanium citrate, J. Am. Ceram. Soc., 82, 1409-1415, (1999). https://doi.org/10.1111/j.1151-2916.1999.tbo1937.x

Jianfei, X., Sakae, T., Shigeo, H., Mikio, S. and Zenbe, N., The thermal decomposition process of barium titanate oxalate tetrahydrate, J. Ceram. Soc. Jpn., 107, 27-30, (1999). https://doi.org/10.2109/jcersj.107.27

Jing, Y. W., Chaolun, L. and Mingmei, W., Double-sided comb-like ZnO nanostructures and their derivative nanofern arrays grown by a facile metal hydrothermal oxidation route, Cryst. Growth Des., 9, 409- 413, (2009). https://doi.org/10.1021/cg8006348

Junhan, Y., Louis, P., Wolfgang, M., Sigmund, J. and Nino, C., Sol-gel based synthesis of complex oxide nanofibers, J. Sol-Gel Sci. Techn., 42, 323-329, (2007). https://doi.org/10.1007/s10971-007-0736-6

Kavitha. R. and Devi, L. G., Synergistic effect between carbon dopant in titania lattice and surface carbonaceous species for enhancing the visible light photocatalysis, J. Environ. Chem. Eng., 2, 857-867, (2014). https://doi.org/10.1016/j/jece.2014.02.016

Lei, C., Yonghong, N., Man, W. and Xiang, M., Magnetic Ni/α-Ni(OH)2 porous superstructures: synthesis, influencing factors and applications in the removal of heavy metals, RSC Adv., 3, 3585-3591, (2013). https://doi.org/10.1039/C3RA22504F

Luis, A. P., Maria, J. D., Francisco, J. G., Maria, J. S., Concepcion, R. and Jose, M. C., Synthesis of needle-like BaTiO3 particles from the thermal decomposition of a citrate precursor under sample controlled reaction temperature conditions, J. Mater. Chem., 13, 2234-2241, (2003). https://doi.org/10.1039/B305828J

Mandal, T. K., Characterization of tetragonal BaTiO3 nanopowders prepared with a new soft chemistry route, Mater. Lett., 61, 850-854, (2007). https://doi.org/10.1016/j.matlet.2006.06.006

Margarita, G., Antonieta, G., Felipe, C., David. J., Genevieve, C., Elder, D. R. and Damien, B., Eu-Doped BaTiO3 Powder and Film from Sol-Gel Process with Polyvinylpyrrolidone Additive, Int. J. Mol. Sci., 10, 4088-4101, (2009). https://doi.org/10.3390/ijms10094088

Marjeta, M. K., Ines, B., Bojan, B. and Danilo, S., The morphology control of BaTiO3 particles synthesized in water and a water/ethanol solvent, J. Am. Ceram. Soc., 96, 3401-3409, (2013). https://doi.org/10.1111/jace.12607

Markus, W., Lewis, W. and Alan, H., XPS analysis of submicrometer barium titanate powder, J. Am. Ceram. Soc., 87, 371-377, (2004). https://doi.org/10.111/j.1551-2916-2004.00371.x

Michael, V., Sanjay, M., Nicolas, L., Volker, H. and Timo. D., Sol-Gel Synthesis of nano-scaled BaTiO3, BaZrO3 and BaTi0.5Zr0.5O3 oxides via single-source alkoxide precursors and semi-alkoxide routes, J. Sol-Gel Sci. Technol., 15, 145-158, (2000). https://doi.org/10.1023/A:1008795419020

Minhua, C., Tianfu, L., Song, G., Genban, S., Xinglong, W., Changwen, H. and Zhong, L. W., Single-Crystal Dendritic Micro-Pines of Magnetica-Fe2O3: Large-Scale Synthesis Formation Mechanism and Properties, Angew Chem. Int. Ed., 44, 4197-4201, (2005). https://doi.org/10.1002/ange.200500448

Miot, C., Husson, E., Proust, C., Erre, R. and Coutures, J. P., X-ray photoelectron spectroscopy characterization of barium titanate ceramics prepared by the citric route residual carbon study, J. Mater. Res., 12, 2388-2392(1997). https://doi.org/10.1557/JMR.1997.0316

Nayak, S., Sahoo, B., Chakia, T. K. and Khastgir, D., Facile preparation of uniform barium titanate (BaTiO3) multipods with high permittivity: impedance and temperature dependent dielectric behaviour, RSC Adv., 4, 1212-1224, (2014). https://doi.org/10.1039/C3RA44815K

Morsi, T. M., Budakowski, W. R., Abd-El-Aziz, A. S. and Friesen, K. L., Photocatalytic Degradation of 1,10-Dichlorodecane in Aqueous Suspensions of TiO2: A Reaction of Adsorbed Chlorinated Alkane with Surface Hydroxyl Radicals, Environ. Sci. Technol., 34, 1018-1022(2000). https://doi.org/10.1021/es9907360

Samanta, P. K., Basak, S. and Chaudhuri, P. R., The secret life of zinc oxide, Mater. Today, 14, 295-315, (2011).

Tapan, K. S. and Andrey, L. R., Nonspherical noble metal nanoparticles: colloid-chemical synthesis and morphology control, Adv. Mater., 22, 1781-1804, (2010). https://doi.org/10.1002/adma.200901271

Vijatoic, M. M., Bobic, J. D. and Stojanovic, B. D., History and challenges of barium titanate: Part II, Sci. Sinter., 40, 235-244, (2008). https://doi.org/10.2298/SOs0803235V

Vivek, P., Babita, B. and Rajender, S. V., Self-Assembly of metal oxides into three-dimensional nanostructures: synthesis and application in catalysis, ACS, 3, 728-736, (2009). https://doi.org/10.1021/nn800903p

Yang, Z., Jianhua, H., Chee, L. M. and Xianhua, W., Effects of site substitutions and concentration on up conversion luminescence of Er3+-doped perovskite titanate, Opt. Express, 19, 1824-1829, (2011). https://doi.org/10.1364/OE.19.001824

Yong, C. Z., Gen, L.W., Kun, W. L., Ming, Z., Xiao, Y. H. and Hao, W., Facile synthesis of submicron BaTiO3 crystallites by a liquid–solid reaction method, J. Cryst. Growth, 290, 513-517, (2006). https://doi.org/10.1016/j.jcrysgro.2006.02.012

Yu-Fong, H., Hung-Shin, S., Chi-Wen, L., Ping, X., Darrick, J. W., Kyle, J. R., Daniel, E. H. and Hsing-Lin, W., Morphology control of Cu crystals on modified conjugated polymer surfaces, Cryst. Growth Des., 12, 1778-1784, (2012). https://doi.org/10.1021/cg201200r

Yury, V. K., Kirill, A. K., Neira, I. S., Takaaki, T., Tadashi, I., Tomoaki, W., Naonori, S. and Masahiro, Y., A novel controlled and high-yield solvothermal drying route to nanosized barium titanate powders, J. Phys. Chem. C, 111, 7306-7318, (2007). https://doi.org/10.1021/jp0678103

Zhang, S., Fusong, J., Gang, Q. and Congyi, L., Synthesis of single-crystalline perovskite barium titanate nanorods by a combined route based on sol–gel and surfactant-templated methods, Mater. Lett., 62, 2225-2228, (2008). https://doi.org/10.1016/j.matlet.2007.11.055

Zhao, C., Krall, A., Zhao, H., Zhang, Q. and Li, Y., Ultrasonic spray pyrolysissynthesis of Ag/TiO2 nanocomposite photocatalysts for simultaneous H2 production and CO2 reduction, Int. J. Hydrogen Energy, 37, 9967-9976, (2012). https://doi.org/j.ijhydene.2012.04.003

Zhao, D., Ying, D., Wen, C., Xinmei, P. and Jihong, L., Synthesis and characterization of bowl-like single-crystalline BaTiO3 nanoparticles, Nanoscale Res. Lett., 5, 1217-1221, (2010). https://doi.org/10.1007/s11671-010-9629-7

Zhibin, L., Jianmin, L., Yugen, Z. and Sheming, L., Fabrication and characterization of highly-ordered periodic macroporous barium titanate by the sol-gel method., J. Mater. Chem., 10, 2629-2631, (2000). https://doi.org/10.1039/B0055554

Zhiqiao, H., Xing, X., Shuang, S., Lei, X., Jinjun, T., Jianmeng, C. and Bing, Y., A Visible Light-Driven Titanium Dioxide Photocatalyst Codoped with Lanthanum and Iodine: An Application in the Degradation of Oxalic Acid, J. Phys. Chem. C, 112, 16431-16437, (2008). https://doi.org/10.1021/jp803291c

Zhou, L., Yu, R., Zhu, K., Yao, J., Xing, X., Wang, D. and Xu, Preparation of plank-like BaTiO3 by hydrothermal soft chemical process from layered titanate precursors, Key Eng. Mater., 336-338, 66-68, (2007). https://doi.org/10.4028/www.scientific.net/KEM.336-338.66